Structures 70 (2024) 107710

Contents lists available at ScienceDirect

Structures

journal homepage: www.elsevier.com/locate/structures

Advancing construction techniques: Textile reinforced concrete shells and high-performance fiber-reinforced concrete beams for partially prefabricated elevated slabs

Marco Carlo Rampini *, Giulio Zani, Matteo Colombo, Marco di Prisco

Politecnico di Milano, Department of Civil and Environmental Engineering, Piazza Leonardo da Vinci, 32 - 20133 Milano, Italy

ARTICLE INFO

Keywords:
High-performance concrete
Precast construction
Fiber-reinforced concrete
Textile reinforced concrete
Lightweight construction
Prefabricated elements
Composite slab
Sustainability

ABSTRACT

Innovative high-performance cementitious materials lead the way for the development of advanced structural systems, characterized by improved durability, mechanical performance, and construction efficiency. In this paper, we introduce a partially precast unidirectional ribbed slab system, featuring very high-performance fiber-reinforced concrete (VHPFRC) I-beams, textile-reinforced concrete (TRC) stay-in-place formworks, and ordinary steel fiber-reinforced concrete (SFRC) finishes. Engineered to maximize the advantages of these innovative materials, the system achieves a lightweight configuration, minimizing the need for on-site steel reinforcement placement. After outlining the conceptual design of the proposed structural system, the paper thoroughly examines the characterization of materials and details the prototyping procedures employed. The theoretical framework is substantiated by an extensive experimental campaign on individual components, offering insights into the full-scale response of the precast elements, and is supplemented by simplified sectional analyses aimed at estimating the flexural behavior of the full composite slab. Additionally, a preliminary assessment of the environmental sustainability of the solution is provided.

1. Introduction

In the evolving world of construction, there is a crucial demand for structural solutions that can adapt to the requirements of contemporary social and technical scenarios. Traditional construction methods are gradually yielding to industrialized solutions, where prefabricated elements [1,2] and modular systems [3] are embraced to ensure precision, shorten construction times and extend the service life of structures. This leads to an increasing need for inventive solutions that incorporate features such as lightweight design [4], ease of assembly, cost-effectiveness, environmental sustainability [5,6] and superior mechanical properties.

In this context, high-performance cement-based composites emerge as highly promising solutions for optimizing various structural components. Expanding upon the pioneering work of Pier Luigi Nervi on ribbed and corrugated systems integrating ferrocement formworks [7,8], this study explores a novel approach for semi-prefabricated elevated slabs. It leverages the mechanical characteristics of advanced cementitious materials, such as very-high performance fiber-reinforced concrete (VHPFRC) [9,10] used in precast I-beams, textile-reinforced concrete (TRC) [11,12] employed in thin-walled shape-resistant shells [13–17], and ordinary fiber-reinforced concrete (FRC) introduced as a cast-in-place topping layer.

The proposed semi-prefabricated system was primarily designed with the aim of achieving a lightweight solution (approximately 3 kN/m^2), exerting positive effects on the entire building structure. Simultaneously, it was engineered for simplicity in the construction process, via the incorporation of modular prefabricated elements and the minimization of extensive on-site operations (e.g. the placement of additional rebar).

This paper, after detailing the technology and materials used, discusses the results of the experimental campaign encompassing different structural components, which have been partially documented in preliminary studies [18,19]. Additionally, it provides a simplified assessment of the flexural response and environmental impact of the full composite slab, deferring refined evaluations, including experimental and numerical analyses, to future studies.

2. Conceptual design of the semi-precast slab

The semi-precast slab of Fig. 1 is composed of an array of VHPFRC structural beams, spaced at 1.15 m intervals with a span of 6 m, coupled

* Corresponding author.
E-mail addresses: marcocarlo.rampini@polimi.it (M.C. Rampini), giulio.zani@polimi.it (G. Zani), matteo.colombo@polimi.it (M. Colombo), marco.diprisco@polimi.it (M. di Prisco).

https://doi.org/10.1016/j.istruc.2024.107710
Received 22 December 2023; Received in revised form 11 August 2024; Accepted 29 October 2024
Available online 11 November 2024

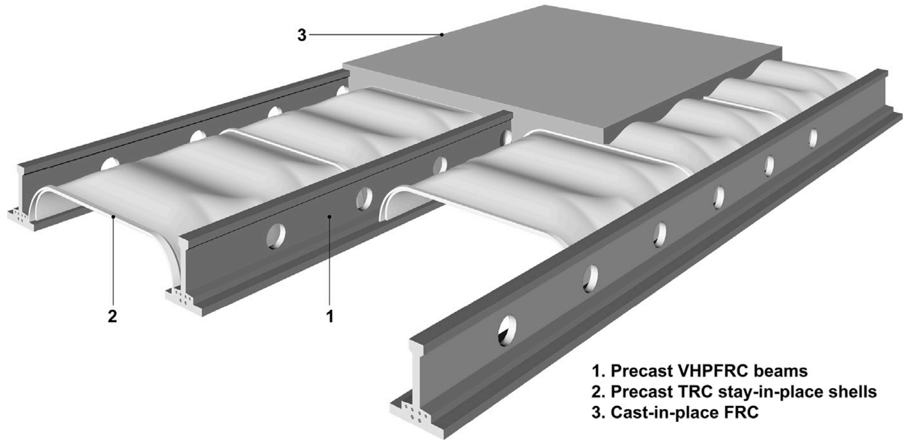

Fig. 1. Scheme of the proposed lightweight elevated slab composed by VHPFRC I-beams, TRC stay-in-place formworks, and ordinary cast-in-place SFRC.
Source: Adapted from [19].

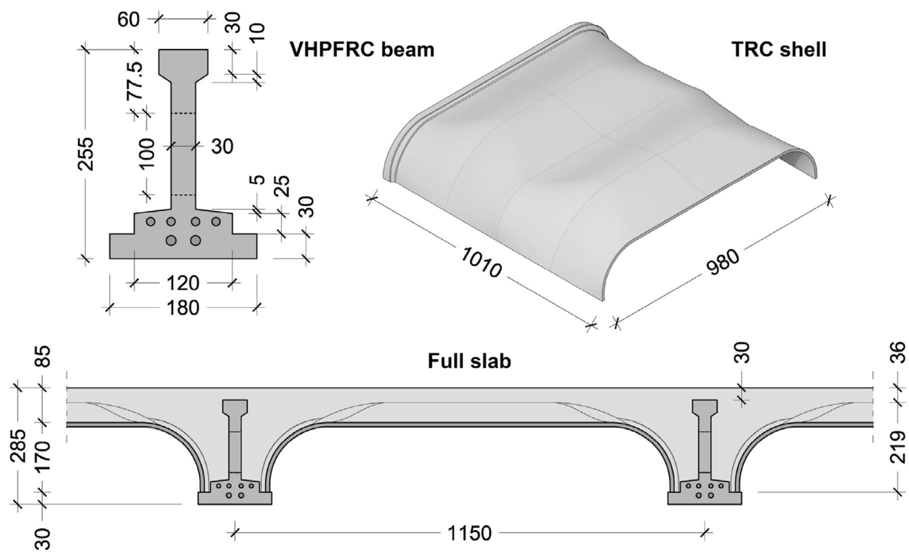

Fig. 2. Details of the proposed slab system: VHPFRC I-beams, TRC shells and full slab section including the cast-in-place SFRC (measures expressed in mm).

with lightweight TRC-based integrated formworks. This configuration reduces weight and enhances structural robustness, positively impacting the overall building structure. Additionally, a cast-in-place steel fiber-reinforced concrete (SFRC) finishing layer is introduced to connect the various structural components, while minimizing the need for on-site rebar placement along the transverse direction. This structural configuration offers several advantages, including: (i) a reduction in overall mass, which in turn results in lower gravitational and inertial loads on structural elements; (ii) enhanced environmental sustainability, due to the lower material usage; and (iii) increased durability, due to the relevant mechanical performance of the materials employed. Moreover, it is expected to shorten construction times compared to a conventionally cast-in-place solution.

Observing the geometry of the VHPFRC beam in Figs. 1 and 2, it is possible to note the total absence of shear reinforcement, achieved by the significant contribution of dispersed steel fibers and two sets of longitudinal reinforcement (four ϕ10 mm and two ϕ12 mm diameter bars). In bending, the beam section is strongly reinforced, with the top reinforcement layer designed to ensure adequate mechanical performance of the whole slab even under fire conditions. In addition, circular holes are introduced along the web of the beams to increase shear transfer between the different structural components and potentially allow for the passage of utilities in the transverse direction.

The purpose of the TRC shell elements (Figs. 1 and 2), similarly to hollow clay bricks in lightened reinforced concrete slabs traditionally employed in Italy, is to reduce dead weights, simplify transient construction phases and allow the longitudinal passage of utilities without interfering with the clear span between storeys. The TRC element has a base of approximately 1 × 1 m^2, a gross depth of 0.22 m, a wall thickness ranging from 6 to 10 mm and a global weight of around 30 kg, making it manually transportable by two operators. Its shape was initially conceived as a cylindrical ellipse, or an extruded omega featuring a flat walking surface. However, both preliminary designs promptly revealed limitations in transient scenarios. To improve the structural performance, alternative geometries leveraging shape and curvature resistance were considered. The optimization process was conducted through preliminary numerical modeling, with a focus on minimizing principal tensile stresses under transient load conditions, ensuring geometric compatibility with the chosen wall reinforcement, reducing the risk of rainwater accumulation on the element, and simplifying production procedures. The preliminary analyses involved evaluating displacements and stresses using linear elastic models. Shell elements, 10 mm thick and incorporating a Simpson thickness integration rule, were used, with an elastic modulus of 45 GPa. The models, representing various design options, were subjected to a central concentrated load distributed over a 100 × 100 mm^2 footprint and were supported unilaterally at the base of the modules.

Table 1
Mix design of the VHPFRC.

Ingredient	Dosage [kg/m^3]
Cement I 52.5	600
Sand 0–2 mm	977
Water	200
Superplasticizer	33
Blast furnace slag	500
Steel microfibers	100

Table 2
VHPFRC uniaxial compression test results; f_c: uniaxial compressive strength.

Specimen	Load [kN]	f_c [MPa]
1	962	125.0
2	1011	131.3
3	995	129.3
Avg (std)	989.3 (25.0)	128.5 (3.2)

As shown in Figs. 1 and 2, prefabricated elements are ultimately topped with a layer of SFRC with a minimum thickness of 30 mm, serving to complete the slab and ensure collaboration between its constituent elements. In the transient phase the self-weight of the fresh SFRC is supported by shells and beams, and in this regard it proved essential to minimize its total volume, i.e. its weight. Under permanent conditions, conversely, the SFRC area becomes important as it predominantly undergoes compressive stresses, thereby counterbalancing the tensile resultant in the flexural mechanism and imparting ductility to the composite section.

3. Materials

As presented, the slab system is based on two prefabricated elements made of high-performance cementitious materials. The I-beams are constructed using VHPFRC, reinforced with traditional ribbed steel bars. The shell elements in TRC are made of a high-performance concrete (HPC), reinforced with a single alkali-resistant (AR) glass fabric. The key mechanical characteristics of these materials are detailed below. Regarding the material for the topping pour, steel fiber-reinforced concrete (SFRC) of class 4b in tension and C45 in compression was selected according to the *fib* Model Code 2010 (MC2010) [20]. This material was not subjected to mechanical characterization tests, as full-scale experiments were conducted solely on the prefabricated parts.

3.1. Prefabricated beams

3.1.1. VHPFRC

The VHPFRC mix design, selected through an extensive optimization process, is detailed in Table 1. The formulation includes a dosage of 100 kg/m^3 of high-carbon steel brass-plated microfibers (length 13 mm, diameter 0.16 mm, aspect ratio approximately 80), corresponding to a 1.2% dosage by volume.

The characterization of the cementitious composite was carried out according to MC2010 [20]. Specifically, the concrete was classified as C120, following uniaxial compression tests on three nominally identical cylinders with a diameter of 100 mm (see Table 2). Regarding the post-peak tensile strength, the material was characterized on three nominally identical notched beams under a center-point loading, according to the EN14651 [21] standard. The results are presented in Fig. 3 and Table 3.

The characteristic values of the flexural residual strengths relevant for serviceability ($f_{R1,k}$) and ultimate ($f_{R3,k}$) conditions were computed using the data from Table 3. They amount to 14.11 MPa and 8.01 MPa, respectively; consequently, the VHPFRC is classified as a 14a material, as per MC2010.

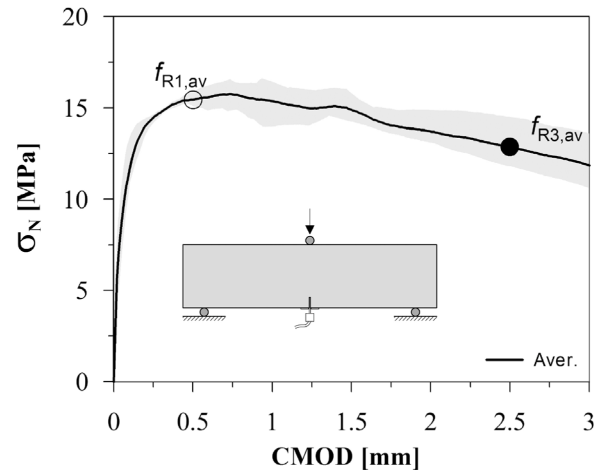

Fig. 3. Flexural response of VHPFRC notched beams: nominal flexural stress (σ_N) vs. crack mouth opening displacement (CMOD) diagrams. Note: the gray solid hatch represent the dispersion of experimental results.

Table 3
Flexural residual strengths of the VHPFRC notched beams; f_{R1} and f_{R3}: residual tensile strengths.

Specimen	f_{R1} [MPa]	f_{R3} [MPa]
1	15.90	14.51
2	15.11	12.27
3	15.38	11.82
Avg (std)	15.46 (0.40)	12.87 (1.44)

3.1.2. Steel rebar

Three nominally identical B450C grade steel ϕ10 mm diameter bars were experimentally tested in uniaxial tension. The mean values of yield strength f_{ym}, yield strain ε_{sy}, ultimate strength f_{um} and ultimate strain ε_{sy} were respectively equal to 534.0 MPa, 0.293%, 626.7 MPa and 12%. Note that, due to the unavailability of ϕ12 mm samples from the same production batch, experiments were conducted exclusively on the ϕ10 mm ones.

3.2. Prefabricated stay-in-place formworks

The TRC was obtained by embedding a layer of alkali-resistant glass double leno weave fabric into a fine-grained high-performance concrete (HPC). The mix design for the HPC was chosen through a procedure focused on achieving optimal workability in the fresh state. This workability criterion was essential for the full-scale production process, which, as will be shown later, entailed pouring the matrix into the casting mold through multiple small openings situated on one side.

3.2.1. Characterization of the base materials

The mix design of the self-compacting HPC is shown in Table 4. The resulting matrix exhibits a water-to-binder ratio of 0.2 and a water-to-cement ratio of 0.36. The maximum aggregate size was reduced to 1 mm to promote a stronger bond between the cementitious material and the coated glass yarns. Relevant mechanical characteristics were assessed through conventional bending and compressive tests on prismatic specimens, following EN 196-1 [22] and MC2010 [20]. The average results obtained from a series of 12 samples measuring 40 × 40 × 160 mm^3 are: bending tensile strength f_{ctf} of 13.5 MPa (std 1.9 MPa), uniaxial tensile strength f_{ct} of 4.7 MPa (std 0.7 MPa) and cubic compressive strength f_{cc} of 100.5 MPa (std 9.3 MPa).

As depicted in Table 5, the chosen alkali-resistant glass fabric, coated with a styrene butadiene rubber (SBR), is characterized by an orthotropic geometry. Specifically, its equivalent thickness t_{eq} is

Table 4
Mix design of the HPC.

Ingredient	Dosage [kg/m^3]
Cement I 52.5	600
Sand 0–1 mm	846.5
Water	214.7
Superplasticizer	55.8
Blast furnace slag	500

Table 5
Characteristics of the AR glass fabric.

Characteristic	
Fabrication technique	Leno weave
Warp spacing [mm]	4.9
Weft spacing [mm]	10.1
Warp yarn [Tex]	2 × 1200
Weft yarn [Tex]	1200

0.183 mm in the warp direction and 0.044 mm in the weft direction, resulting in a strength ratio of approximately 4:1. According to Colombo et al. (please refer to fabric F3 in [23]), the average tensile capacity in the warp direction is 157.4 kN/m. Consequently, a maximum load of approximately 39.4 kN/m shall be expected along the weft.

3.2.2. Tensile response of the composite

In order to analyze the tensile characteristics of the composite in the two primary fabric weaving directions, uniaxial tensile tests were conducted on six specimens with nominal dimensions of 9 × 70 × 400 mm^3. Three coupons featured a fabric oriented in the weft direction, while the remaining three had a fabric arranged in the warp direction. In all instances, the fabric was centrally placed within the sample thickness and a hand lay-up technique was used for casting.

The tests were carried out using constant displacement control at a fixed rate of 0.02 mm/s. Four steel plates, 2 mm thick and measuring 50 × 70 mm^2, were glued to the specimens ends to ensure a more uniform distribution of pressure applied by the grips (clamping force of approximately 8 kN). Additionally, two LVDT (linear variable differential transformer) sensors were applied, one at the front and one at the back of each specimen, to measure the relative crack opening displacements (COD) over a nominal gauge length of 200 mm. The nominal free length L_0 of the specimens was 300 mm.

The experimental curves for the nominal tensile stress (σ_N) vs. normalized stroke displacement (δ/L_0) are depicted in Fig. 4. The individual responses are presented in black alongside the red average behavior, both in the warp (Fig. 4a) and weft (Fig. 4b) reinforcing directions. It is important to note that the reported nominal stresses were computed by dividing the load measured by the load cell by the actual cross-sectional area of each composite. Fig. 4 also features the crack patterns of all six specimens; it can be observed that all of them displayed multiple cracks before reaching failure, except for the weft-N$_{01}$ specimen, which fractured near the steel plate due to the loss of adhesion between the fabric and the matrix, potentially caused by a localized manufacturing defect. As a result, the test was interrupted and the following part of the graph is omitted. It is noteworthy that the TRC exhibited a maximum in-plane tensile stress of approximately 15 MPa and 5 MPa in the warp and weft directions, respectively. This asymmetry can be attributed to the intrinsic characteristics of the glass fabric detailed in Table 5.

3.2.3. Flexural response of the composite

Given the stress conditions expected in TRC shells, especially under transient situations that may involve out-of-plane actions, the decision was made to investigate the flexural behavior of the TRC through 12 bending tests on specimens with nominal size of 15 × 70 × 500 mm^3. These specimens were obtained by sawing a larger plate that was cast alongside the full-scale shells. Six specimens were cut along the weft fabric direction, and six along the warp. However, it is crucial to note that the positioning of the reinforcing fabric within the thickness of the large plate could not be controlled during the casting process. Considering the potential sub-optimal positioning in the full-scale shells as well (see Section 4), for each direction it was decided to evaluate three bending specimens with the fabric placed in the tensile zone and three with the fabric positioned near the top chord of the cross-section.

The experiments employed a four-point bending setup, with a 450 mm distance between supports and a nominal shear span of 150 mm. Since the flexural specimens were unnotched, four displacement transducers (LVDT) were arranged as follows: two positioned on the bottom surface of the specimen, with a nominal gauge length of 200 mm, and two smaller LVDTs on the top surface, spanning a gauge length of 40 mm. The tests were conducted by controlling the displacement of the loading knives at a constant speed of 0.002 mm/s. However, for the specimens tested with the fabric positioned near the top edge, a brittle behavior was observed. Therefore, after the initial cracking occurred, the testing rate was increased to 0.004 mm/s.

As predictable, the placement of the AR glass fabric within the sample thickness significantly affected the flexural response (Figs. 5 and 6, displaying the nominal flexural stress vs. stroke displacement diagrams). This impact was further accentuated by opting for a statically determinate testing arrangement, which precluded the activation of membrane mechanisms, minimizing the contribution of the fabric in cases of limited internal lever arm.

The warp-N$_{01}$, warp-N$_{02}$, and warp-N$_{04}$ specimens, with the fabric positioned in the tensile zone (refer to the cross-sections at the failure locations investigated through machine sawing in Figs. 5 and 7a), consistently exhibited the ability to withstand higher loads after the initial cracking, owing to the characteristic trilinear strain-hardening behavior of TRC. This provided evidence of the effectiveness of the reinforcement, resulting in a peak flexural stress of approximately 30 MPa, which varied depending on the number of intact glass rovings remaining after the sample extraction. In contrast, specimens warp-N$_{03}$, warp-N$_{05}$, and warp-N$_{06}$, which had the fabric positioned near the top edge, experienced a loss of equilibrium after the initial cracking. Only warp-N$_{03}$ demonstrated some residual strength, attributed to its ability to develop a modest flexural capacity (as clearly seen in the cross-section of Fig. 5). It is worth noting that warp-N$_{03}$ was the only sample in the set with an effective reinforcement depth of a few millimeters.

Similar behaviors are evident in the weft direction (Figs. 6 and 7b). However, it is crucial to note the absence of a typical trilinear behavior in the weft-N$_{01}$, weft-N$_{02}$, and weft-N$_{03}$ specimens. In this case, the pronounced strain-hardening was not observed due to the lower reinforcement ratio in the weft direction.

The crack patterns on the bottom surfaces of the 12 flexural specimens are depicted in Fig. 7. These images provide a clear insight into the distinct fracture mechanisms – and, consequently, the different potential for strain energy dissipation – based on the location of the AR glass fabric within the depth of the composite.

4. Prototyping of prefabricated elements

In order to verify the feasibility of prefabricated elements and test their individual full-scale mechanical performance, the prototyping of two VHPFRC beams and two TRC formworks was carried out. The beams were produced using a reusable timber formwork, with surfaces in contact with fresh concrete treated to minimize the use of shuttering oil. To prevent shrinkage cracking, particularly significant in the selected matrix (long-term shrinkage strain $\varepsilon_{sh,\infty}$ is estimated at approximately 1‰), the lateral surfaces of the formwork were removed after about 24 h of curing at laboratory conditions. As shown in Fig. 8a, the self-compacting self-leveling concrete was slowly poured from the top, preventing a pronounced orientation of fibers in the longitudinal direction but ensuring complete filling. Note that reinforcement bars

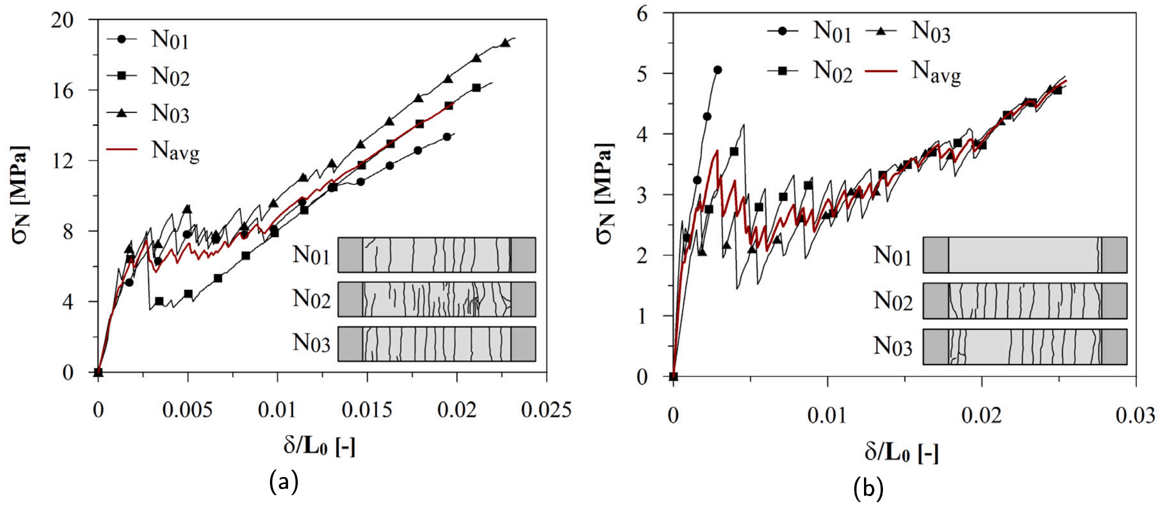

Fig. 4. Tensile tests responses in terms of nominal composite stress (σ_N) vs. normalized displacement (δ/L_0) in the warp (a) and the weft (b) directions. Note that in case of the loss of a specimen, red curves continue by averaging the results of remaining samples. (For interpretation of the references to color in this figure legend, the reader is referred to the web version of this article.)
Source: Adapted from [19].

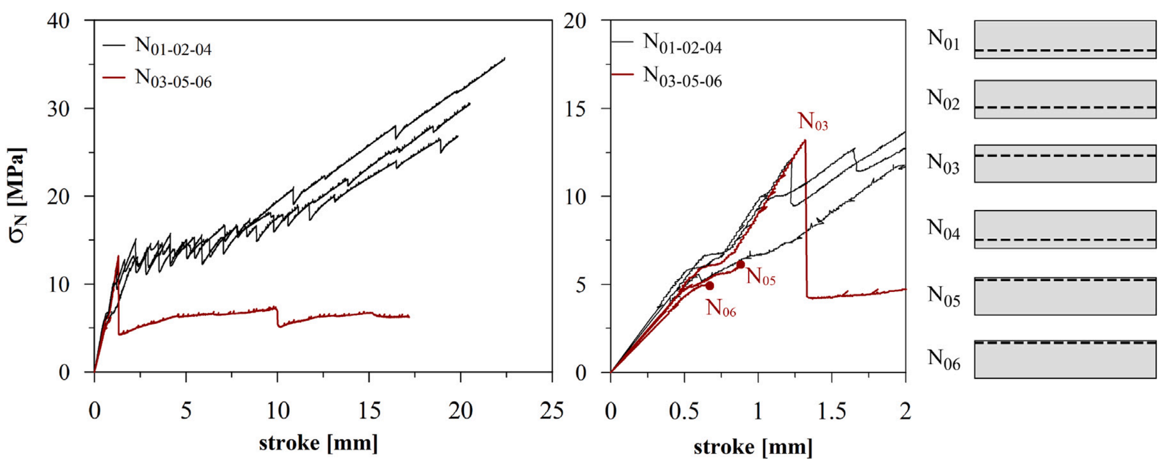

Fig. 5. Nominal flexural stress (σ_N) vs. stroke curves for the warp-oriented TRC coupons and zoom in the 0–2 mm stroke range. Cases with the textile positioned upwards are identified in red. Pictures of the 15 × 70 mm^2 TRC nominal cross-sections displaying the fabric position at the failure region are also included. (For interpretation of the references to color in this figure legend, the reader is referred to the web version of this article.)
Source: Adapted from [19].

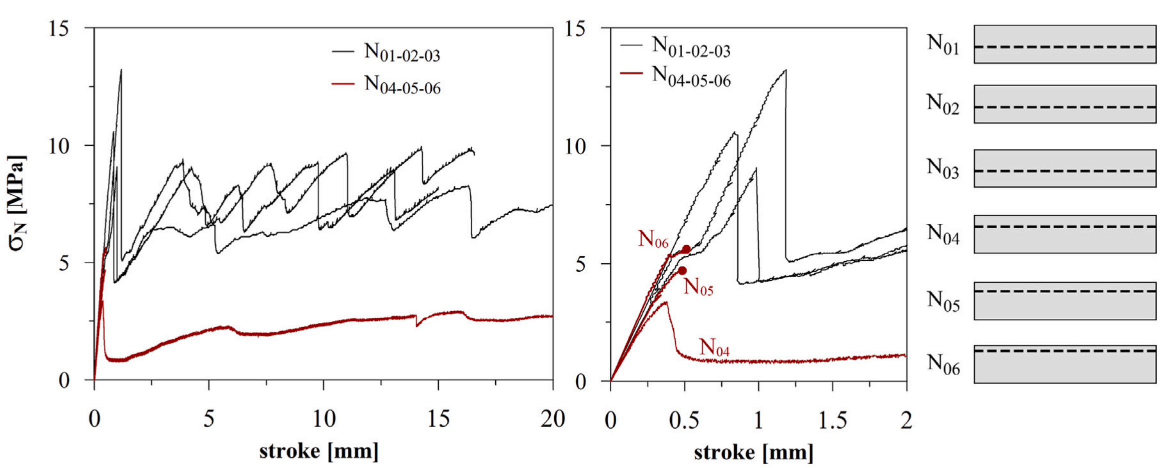

Fig. 6. Nominal flexural stress (σ_N) vs. stroke curves for the weft-oriented TRC coupons and zoom in the 0–2 mm stroke range. Cases with the textile positioned upwards are identified in red. Pictures of the 15 × 70 mm^2 TRC nominal cross-sections displaying the fabric position at the failure region are also included. (For interpretation of the references to color in this figure legend, the reader is referred to the web version of this article.)
Source: Adapted from [19].

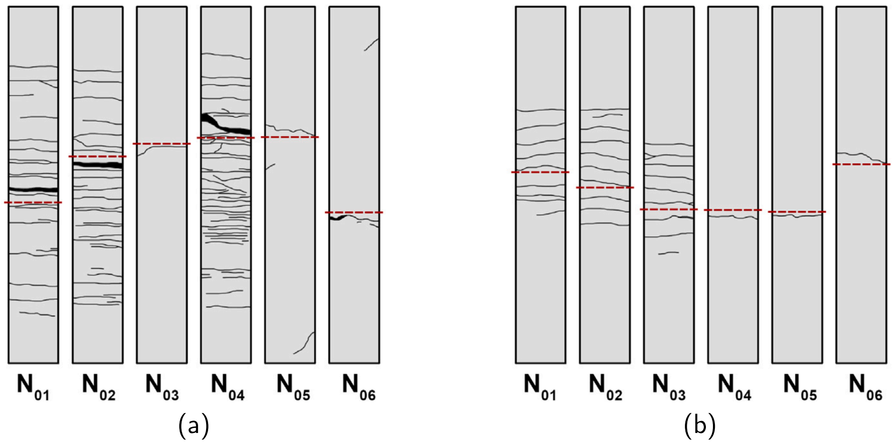

Fig. 7. Crack patterns on the tensile face of the (a) warp and (b) weft flexural specimens. Note: the red dashed line represents the post-failure sawing section.

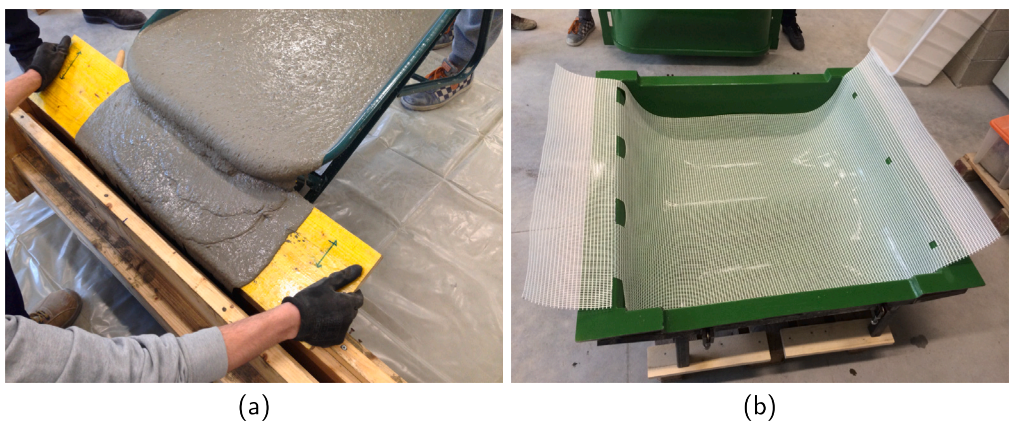

Fig. 8. Casting of the VHPFRC beam from the top of the timber formwork (a), and positioning of the AR glass fabric in the negative fiberglass mold before assembling and casting (b). In the background, the positive mold is partially visible, ready to be inserted.

were positioned at the bottom of the formwork before the solidarization of its different parts. In the first beam (B_{01}), an undesirable bowing of the two lateral boards of the timber formwork was observed. This effect, more prominent in the central section, resulted from the hydrostatic pressure exerted by the freshly poured VHPFRC and implied a slight variation in the geometry of Fig. 2 (the upper width increased from 60 mm to about 70 mm), corrected in the second beam cast through the use of contrasting elements.

The TRC element was similarly prototyped, using a double reusable fiberglass mold (Fig. 9), manufactured with computer numerical control (CNC) techniques, based on the final geometry of the TRC shell. Also in this case, surfaces in direct contact with the HPC were superficially treated to ensure a smooth finish. The glass fabric was placed on the negative mold (Fig. 8b), orienting the warp in the direction of the maximum principal tensile stresses (transverse direction of the slab) numerically estimated in transient phases. The insertion of the positive mold, tightened to the structure of the first element (Fig. 9), facilitated the draping of the AR glass fabric onto the complex shell geometry; it is emphasized that, in this case, it was decided not to impose the placement of the fabric halfway through the TRC wall thickness, mainly relying in transient phases on the activation of membrane behaviors. As shown in Fig. 9, openings were provided on the surface of the positive mold for the pouring of the HPC matrix and for venting the trapped air. At the end of a 24-h curing phase, the positive mold was removed, and the prototype was extracted, preventing the formation of restrained shrinkage damage. Finally, the overlap of the elements displayed in Fig. 1 was verified by superimposing the two TRC shell prototypes.

5. Full-scale tests on VHPFRC beams

In order to evaluate the capacity of the VHPFRC beam, two four point bending tests and four center-point loading shear tests were conducted. Test setups and mechanical results are reported below.

5.1. Bending tests

Two four-point bending tests were carried out on two nominally identical 3.4 m long VHPFRC beams, each featured with three 100 mm diameter circular holes with a 200 mm spacing (Fig. 10). These holes were introduced to explore the possibility of ensuring a transverse passage for utilities (in combination with specifically designed TRC shells) and to enhance shear transfer between the different components of the slab. They were included in the test on the individual component to rule out potential impacts on the flexural response, despite their placement in the region of minimum (theoretically zero) shear force.

The total span was fixed at 3.2 m and the loading knives were positioned at 1.3 m from the supports, leading to a constant bending moment zone of 0.6 m. Vertical displacements were monitored by means of three potentiometric displacement transducers (PDTs) placed at the mid-span and at the loading knives locations. Readings $\delta_{1,2,3}$ were measured as relative displacements from a horizontal steel bar hinged at points C in Fig. 10. Longitudinal relative displacements at top and bottom fibers of the beam, respectively measuring the axial shortening (COM) and elongation (integral crack opening displacement, COD), were monitored using four LVDTs (2+2, front and back). The uniformly

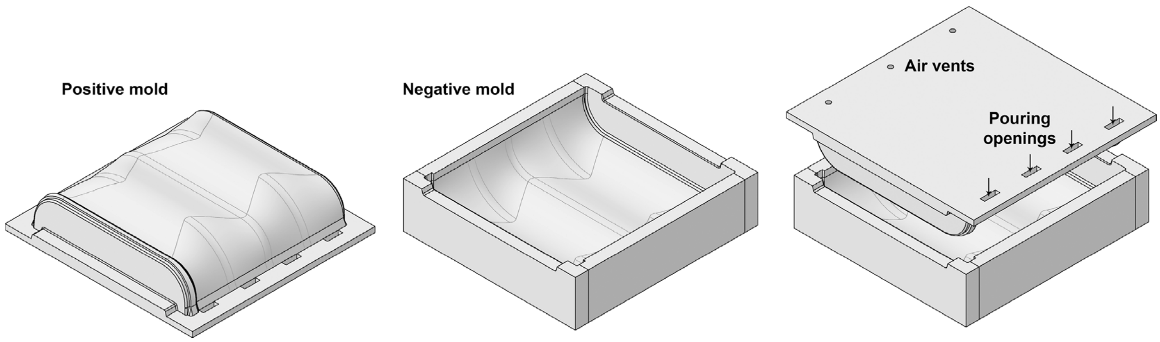

Fig. 9. Schematic representation of the fiberglass formwork used for prototyping the two TRC shells. From left to right: positive mold, negative mold, and assembly by inserting the positive mold into the negative one.

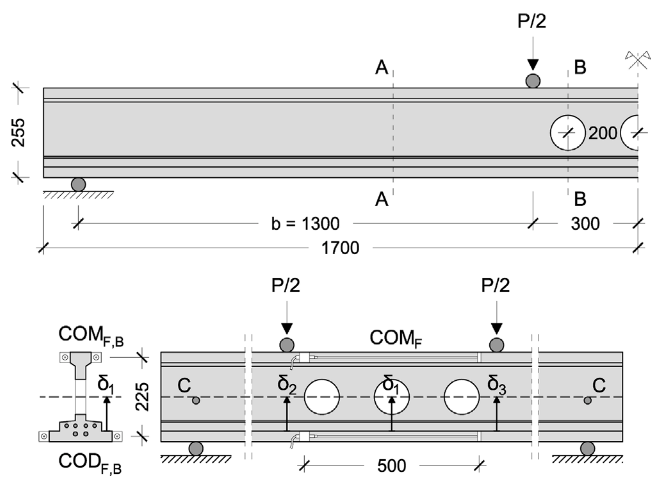

Fig. 10. Four-point bending test setup, nominal geometry of the VHPFRC-beam and instruments arrangement.

distributed strains, $\varepsilon_{COM,COD}$, were then estimated by dividing COM and COD readings by the gauge lengths, nominally equal to 500 mm.

The first beam, B_{01}, was tested under load control up to 90 kN, at a rate of 25 N/s. Then, after the unloading phase, the test progressed in displacement control at a 0.08 mm/s rate. Conversely, the second one, B_{02}, was directly tested under displacement control, setting the head actuator displacement velocity at 0.035 mm/s. The results of the two tests are reported respectively in terms of load vs. mid-span displacement and moment vs. curvature in Fig. 11; axial shortening and elongation are depicted in Fig. 12. The curvature in the middle zone of the beam was computed as the ratio between the sum of $|\varepsilon_{COM}|$ and ε_{COD} and the vertical distance between top and bottom LVDTs, equal to 225 mm, as visible in Fig. 10. Note that the values plotted in Fig. 12 were obtained by averaging front and back measurements.

Both the tests revealed the brittle compression failure of the top bulb at 96.8 kN and 89.2 kN, respectively for beams B_{01} and B_{02}; this result is consistent with the significant geometric reinforcement ratio of the structural element. In Fig. 11a, a detail of the failure mode is reported for the B_{02} case. Specimen B_{01} displayed a broader ductile branch before failure, which can be attributed to the unintentional 10 mm enlargement of the top section width, as previously mentioned in Section 4. While brittle failure in compression is generally not recommended in a structural beam, it can be deemed acceptable for the specific case because it is expected to be active only under transient conditions. In the final stage, in fact, the VHPFRC beams operate within the composite slab alongside the integrated cast of SFRC, as explained in Section 2. Discussion of the behavior of the composite elevated slab is provided in Section 7.

The influence of the larger width in beam B_{01} is also confirmed by the experimental response in terms of moment vs. top axial shortening (COM). In fact, greater deformability is evident in the B_{02} case (Fig. 12a), and this is also slightly reflected in the moment vs. curvature diagram (Fig. 11b).

Fig. 13 documents the crack patterns traced at the end of the two tests on both the front and back side of the beams. Despite the limited differences observed in the structural response diagrams, a different crack pattern was obtained. In particular, in the second case, a larger number of shear cracks developed on one of the two sides of the specimen. This variation, which will be the subject of future in-depth investigation through advanced nonlinear numerical analyses, may be attributed to the combined effect of testing procedures, geometrical variability, and uneven distribution of short fibers during the casting. As can be observed in the figure, the three holes represent a minor defect, as the cracking pattern appears locally altered, and the flexural failure occurred in both cases at the location of a hole.

5.2. Shear tests

Four preliminary shear tests were performed on beam specimens extracted by sawing the 3.4 m long beams along the dashed line A-A of Fig. 10, following the bending test and avoiding interaction with pre-existing cracks as much as possible. In this case, the holes were not included, as it is expected that in the actual solution no holes will be present near the supports. However, detailed studies would still be required to precisely determine the placement of the holes on the 6-meter precast element, considering real load configurations.

Three-point bending tests were carried out, setting the span at 0.7 m (shear span 0.35 m), under displacement control up the reaching of the brittle failure. The peak loads recorded during the tests were 99.2 kN and 77.8 kN in segments 1A and 1B (beam B_{01}), and 74.2 kN and 66.5 kN for the specimens obtained from beam B_{02}. Examining the segments at the end of the tests (see Fig. 14), only specimen 2A exhibited a typical shear failure. In the samples extracted from beam B_{01}, the peak capacity was attained by local crushing beneath the loading knife. In case of segment 2B, caution is advised regarding the peak value, due to the diffuse cracking developed during bending test.

6. Full-scale tests on TRC formworks

The lightweight TRC-based stay-in-place formworks serve a dual purpose: redistributing the surface loads (e.g. the self-weight of the fresh SFRC) to the VHPFRC I-beams and ensuring the safe passage of the operators during the transient assembling phases. The latter condition represents the most critical scenario for the TRC shells, as they are subjected to localized point-loads associated with the walking action of workers. For this reason, two experimental tests were carried out with the aim to assess the capacity of the formwork to withstand the expected actions, which correspond to 1.2 kN distributed over a

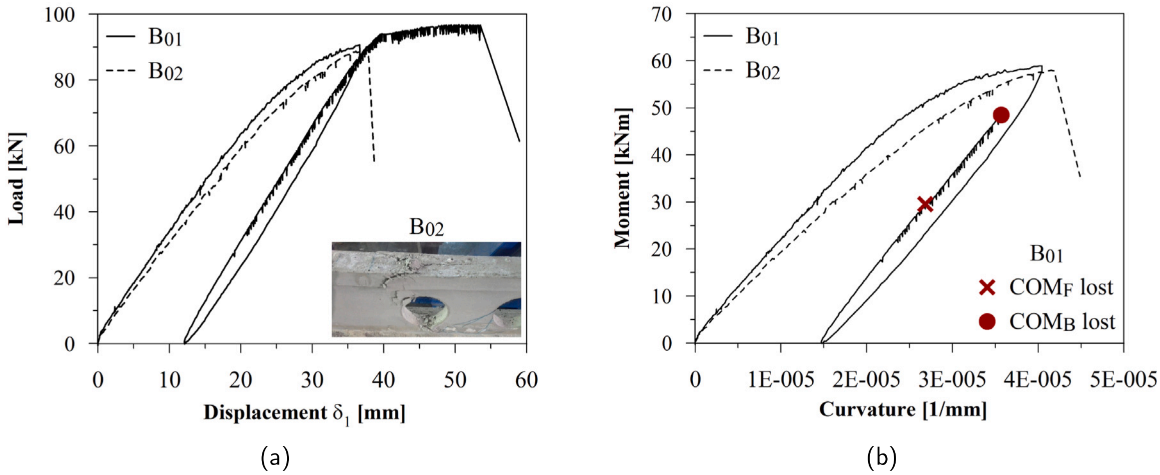

Fig. 11. Results of the VHPFRC beam bending tests in terms of load vs. mid-span displacement, δ_1 (a) and moment vs. curvature (b). A detail of the top bulb failure of sample B_{02} is also provided.

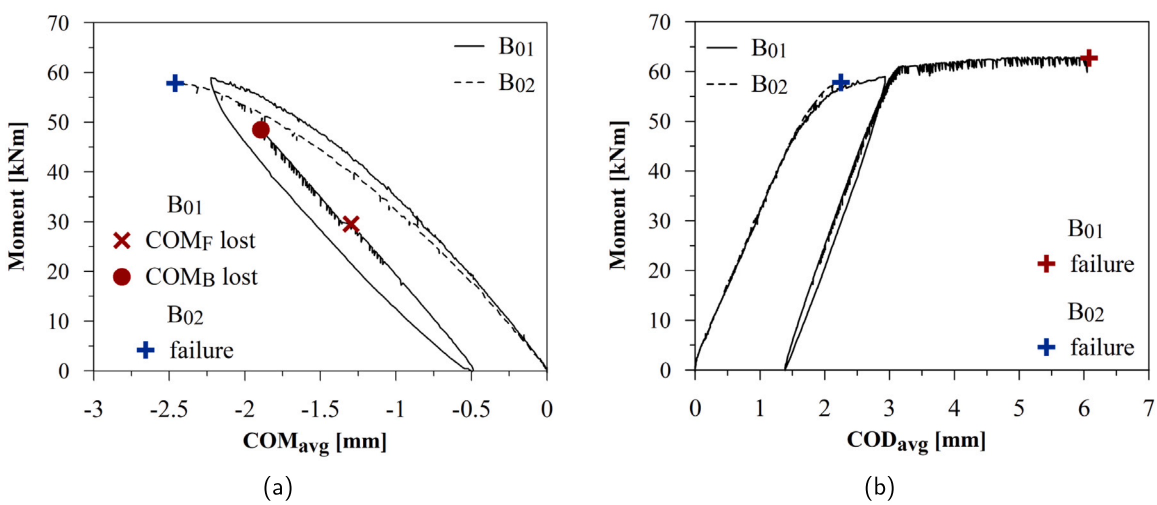

Fig. 12. Results of the VHPFRC beam bending tests in terms of load vs. axial shortening, COM (a), and load vs. axial elongation, COD (b).

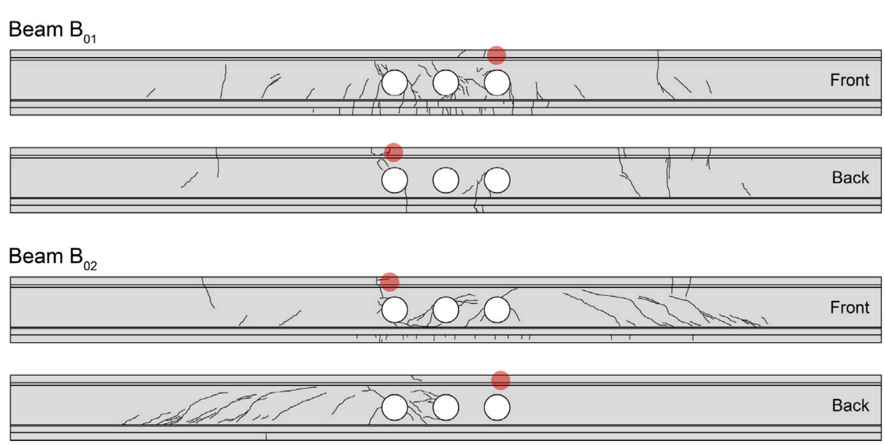

Fig. 13. Crack patterns on the front and back faces of the beams at the end of the tests. Red dots identify the compressive failure locations. Note that, as only cracks recognizable by visual inspection were marked, the potential presence of micro-cracks cannot be excluded. (For interpretation of the references to color in this figure legend, the reader is referred to the web version of this article.)

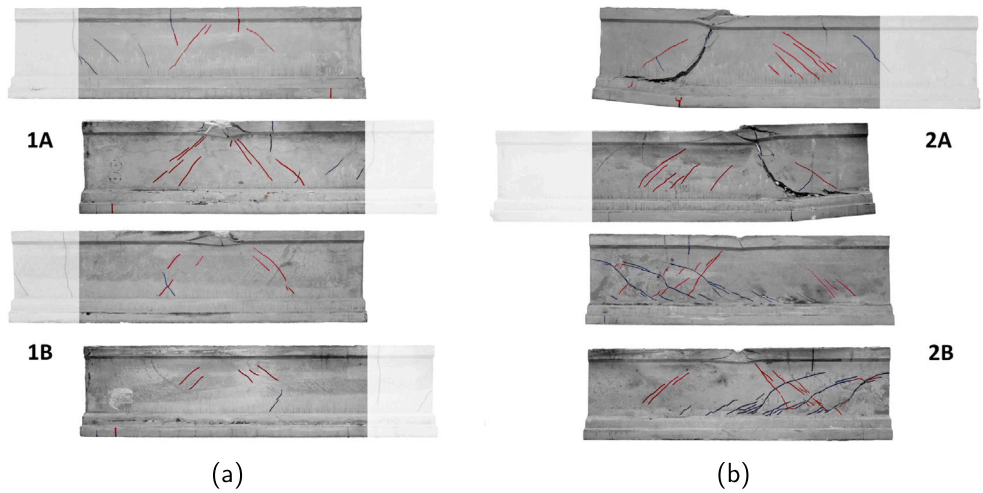

Fig. 14. Crack patterns on the front and back faces of the beam segments at the end of the shear tests: (a) samples 1A, 1B and (b) samples 2A and 2B. Note: pre-existing flexural cracks are traced in black, while shear cracks are traced in red. (For interpretation of the references to color in this figure legend, the reader is referred to the web version of this article.)

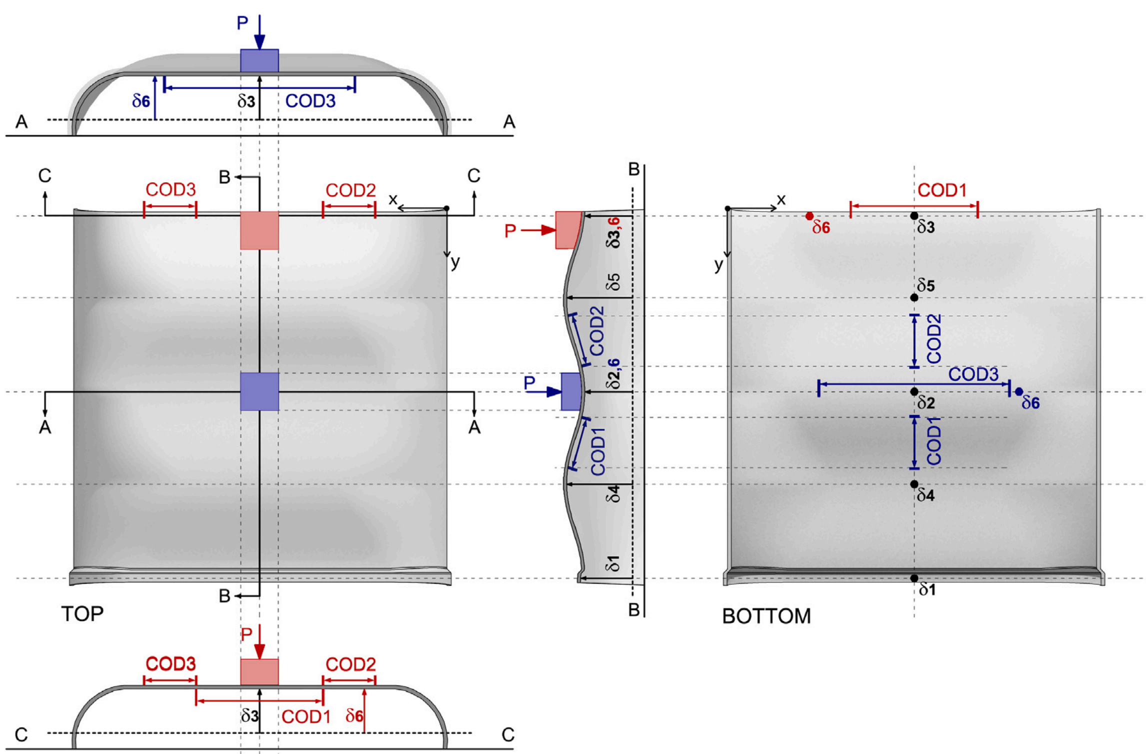

Fig. 15. Test setup and instruments arrangement. Load (P), δ_6 and COD$_{1-3}$ positions refer to centered (blue) and eccentric (red) load tests. Please note that the warp direction of the AR glass fabric was oriented parallel to the x-axis. (For interpretation of the references to color in this figure legend, the reader is referred to the web version of this article.)
Source: Adapted from [19].

100 × 100 mm^2 equivalent footprint, in accordance with mandatory standards. In the two tests the load was applied alternatively in a centered and an eccentric position, as visible in Fig. 15, representing the most challenging transient conditions for the shell. Note that, to precisely apply the point-loads on the extrados surface, a CNC custom-shaped wooden block was carefully positioned on the top surface of the shells (see Figs. 16a and 19). In both the tests, the load was introduced by imposing a constant increase of stroke equal to 0.001 mm/s, with the aid of a loading frame equipped with an electro-mechanical actuator with a capacity of 1000 kN. To precisely monitor the acting load, a 5-kN piezo-resistive load cell was also interposed and screwed to the top of the wooden blocks.

Six PDTs and three LVDTs were used to monitor respectively the vertical displacements and the relative displacements along selected reference points on the TRC surface (identified also as crack opening displacement, COD). Five PDTs were placed under the point-load and at each rib of the shell along the axis of symmetry (δ_{1-5}), while one PDT was used to capture the transverse behavior (δ_6). The three LVDTs were arranged to monitor the sequential formation of cracks close to the load application area, consistently with the results of preliminary numerical analyses. Note that, as visible in Fig. 15, two alternative configurations of transducers were implemented to adequately monitor the shell response as a function of the point of load introduction. To replicate the actual boundary conditions, the TRC formworks were strategically positioned on two segments of VHPFRC I-beams, matching the design of the full composite slab. The results of the two mechanical tests are reported in the following.

6.1. Centered load test

The results of the centered test in terms of load vs. displacement, load vs. COD, and crack pattern development are reported in the following (see again the centered test setup in Fig. 15). As one should note, the shell exhibited an almost linear response over the nominal 1.2 kN load (see P-δ curves in Fig. 17), thereby confirming the fulfillment of the minimum capacity requirement. The $COD_{1,2}$ outputs, reported in Fig. 18a, remained close to zero up to a level of load of about 2.5 kN, demonstrating the reversible behavior of the shell in this load range. Conversely, the COD_3 exhibited a limited opening since a lower load was applied; this was probably caused by the presence of pre-existing micro-cracks and trapped air bubbles related to the prototyping operations. After reaching the maximum load cell capacity (i.e. 5 kN), the prototype was unloaded and all the on-board instruments removed. Subsequently, the test was carried out with the same stroke rate, monitoring the force with the 1000 kN cell connected to the jack. As the maximum capacity of around 5.8 kN was attained (nearly five times the nominal load), a softening behavior characterized by the progressive tearing of the AR glass fabric and the ejection of the matrix (see Fig. 16b) was triggered.

The overall behavior of the shell was mainly governed by the development of membrane stresses; in fact, even if permanent deformations were recorded after the unloading-reloading phase, no significant damage of the fabric carrying in-plane stresses was identified before the response peak, as confirmed by the limited COD values at peak and the modest crack development (see Fig. 18). The results of the test in terms of load vs. vertical displacements, Fig. 17b, show the non-symmetrical response of the formwork; the presence of a stiffer overlapping zone led to a lower vertical displacement than of the opposite side (δ_1 against δ_3) and the absence of cracks (see Fig. 18b). This confirms the choice of considering point-load application at eccentric position as the most critical for the TRC shell response.

6.2. Eccentric load test

As for the centered position, the results of the eccentric test are reported in terms of load vs. displacement, CODs and crack pattern. The response of the shell remained linear-elastic up to the reaching of 1.4 kN (linear P-δ and zero crack opening, Figs. 20 and 21a), load at which a main crack was formed (see Fig. 21b). Then, the maximum prototype capacity of 2.0 kN was attained (over 1.5 times the required nominal load), undergoing a sequential formation of plastic hinges (light blue cracks in Fig. 21); this proves the activation of a membrane behavior which took over a rather poor flexural capacity caused by the possibly incorrect positioning of the fabric within the wall thickness. The evolution of COD readings, exhibiting opening, closure, and subsequent re-opening during the test (Fig. 21a), attests the evolution of the crack pattern (Fig. 21b). Note that COD_1 reading was lost due to an electrical connectivity issue. The test was arrested at around 60 mm of stroke, corresponding to a significant rotation of the prototype (opposing readings from PDTs on opposite sides, δ_1 and δ_3) and to the tearing of the textile across the main crack (see Fig. 19b).

7. Simplified sectional analyses and insights into the full composite solution

In this section, the bending behavior of the VHPFRC beam is estimated by means of a plane-section approach and compared with the experimental results previously presented. Subsequently, the analytical procedure is extended to simulate the entire composite slab, aiming to assess its structural performance under bending actions. The main assumptions on geometry and constitutive laws are presented in the following, together with the obtained results. Finally, preliminary considerations on the sustainability of the proposed solution are discussed, with reference to traditional floor systems.

7.1. Validation on the VHPFRC beam

In order to better understand the experimental behavior of the VHPFRC beams reported in Section 5, simplified analyses were performed under the typical assumption of a plane-section kinematic model. Regarding materials behavior, a bilinear curve was taken for the steel bars (same law for both diameters), while compressive and tensile constitutive laws of the VHPFRC were determined according to the formulations proposed by the *fib* Model Code 2010 [20]. A Sargin-type compressive curve was derived from the mean cylindrical compressive strength, f_{cm}, and a simplified piecewise-linear tensile law was obtained from the average residual strengths, f_{Fts} and f_{Ftu}, introducing a characteristic length, l_{cs}, to calculate equivalent tensile strains ($\varepsilon = w/l_{cs}$) from corresponding crack openings w. The adopted l_{cs} corresponds to a crack spacing equal to 45.4 mm, calculated by means of well-proven Italian Standards [24]. Despite the common knowledge that relevant dosages of short fibers positively affect the uniaxial compression post-peak behavior of high-strength concretes, precautionary assumptions suggested to omit the softening branch in this analysis. In fact, phenomena such as fibers segregation within the mold can significantly reduce the volume fraction at the top section layer, implying a sudden rupture of the cement-based material after reaching the peak strength, as holds in plain concrete. In order to assess the suitability of the plane-section approach in replicating the experimental response, average values of the mechanical parameters reported in Section 3 were used. Note that, due to the uneven increment of the top bulb width in the casting of the first VHPFRC beam (B_{01}, described in Section 5), only the behavior of the second one, B_{02}, is taken as reference. The analytical moment vs. curvature was computed by iteratively writing sectional equilibrium equations and integrating the stress distributions over the beam depth. The assumptions of plane-section and perfect bond between concrete and steel rebar were considered, together with the previously described constitutive laws and the member nominal geometry. The results of the computation are reported in Fig. 22, both for the running solid section and for the one corresponding to the hole (see sections A-A and B-B Fig. 2). It is worth noticing that no substantial differences were found between the two, and a peak moment capacity, M_u, equal to around 64 kN m was estimated for the B-B section (around 10% larger than the experimental result discussed in Section 5). A brittle failure associated with the rupture of the top bulb in compression was identified, following a very limited yielding of the bottom steel bars. As above mentioned, this failure mode was assumed acceptable, since in the proposed slab technology the VHPFRC beams are intended to be working as components of a composite section, together with the cast-in-place SFRC (see Fig. 1).

The analytical response adequately reproduces the ultimate capacity and failure mechanism, but a strong difference in the first branch stiffness can be observed. This phenomenon is probably due to the constrained shrinkage of the cement-based material, which occurs during the hardening and curing phases, leading to pervasive micro-cracking. This effect could be induced by the interaction with the longitudinal rebar and the intricate geometry of the element. In order to take it into account, the analytical procedure was refined by imposing a uniform shrinkage strain distribution ($\varepsilon_{sh} = 1 \cdot 10^{-3}$) to the VHPFRC. The refined moment vs. curvature response reported in Fig. 22 for the B-B section confirmed the hypothesis, leading to lower discrepancies on the estimation of both the ultimate capacity (M_u = 61.6 kN m, error of around 6%) and the initial stiffness. Considering the experimental equilibrium scheme, the analytical ultimate shear, V_u, corresponding to the peak bending moment was equal to 47.4 kN (M_u divided by the experimental shear span). The discrepancy between the

Fig. 16. Picture of the centered load test setup (a) and detail of the failure mode at the end of the test (b).

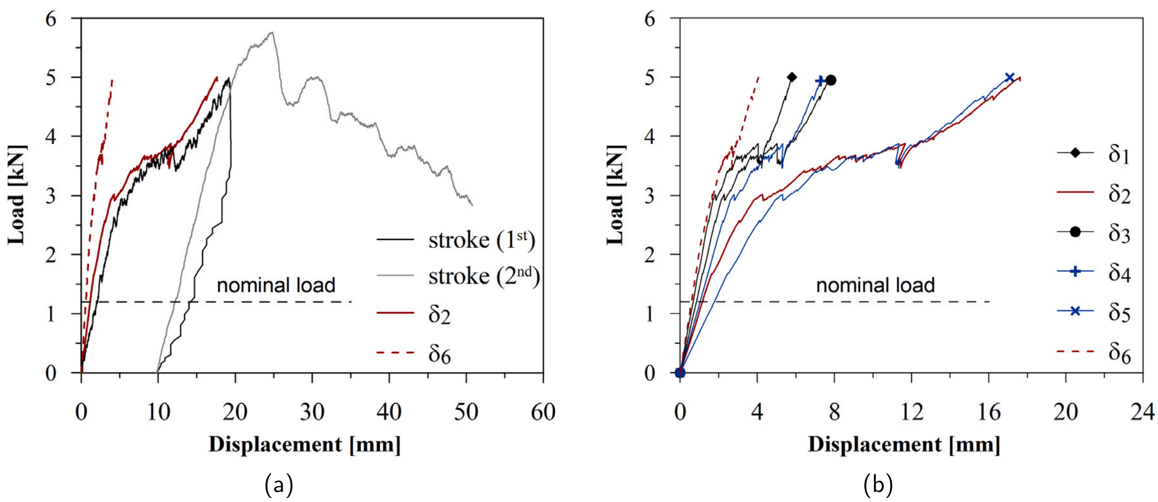

Fig. 17. Load vs. displacement curves of the centered load test: comparison between the stroke and $\delta_{2,6}$ (a), and plot of all δ_{1-6} (b).
Source: Adapted from [19].

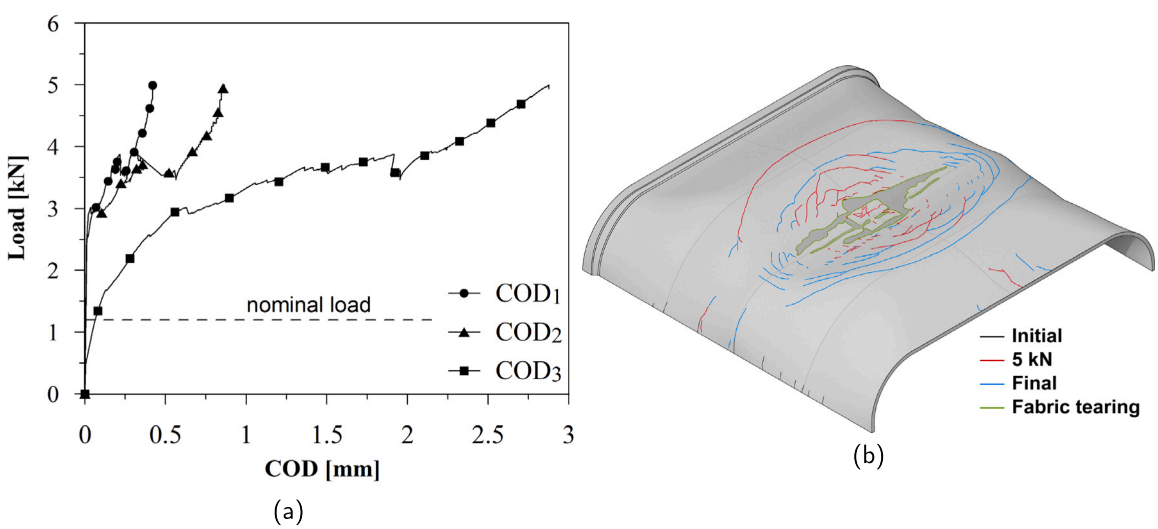

Fig. 18. Centered load test results: load vs. CODs (a) and crack pattern evolution during the test (b). (For interpretation of the references to color in this figure legend, the reader is referred to the web version of this article.)
Source: Adapted from [19].

refined curve and the experimental response of the central part of the beam, concerning the moment–curvature relationship, underscores the limitations of the employed plane-section assumption. Specifically, the kinematic model fails to simulate the longitudinal slip between the upper (compressed) and lower (tensioned) segments of the beam, especially in the region affected by the presence of web holes. The observed shear cracking around the holes, as depicted in Fig. 13, validates the necessity to incorporate such an effect for an accurate

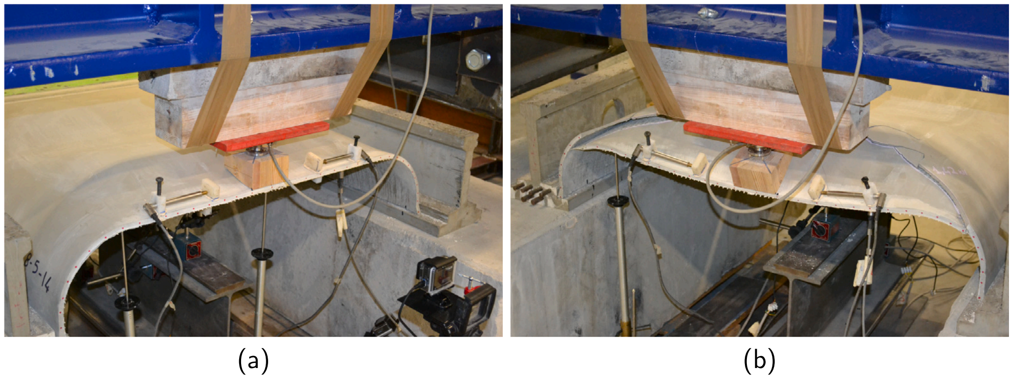

Fig. 19. Picture of the eccentric load test setup (a) and detail of the failure mode at the end of the test (b).

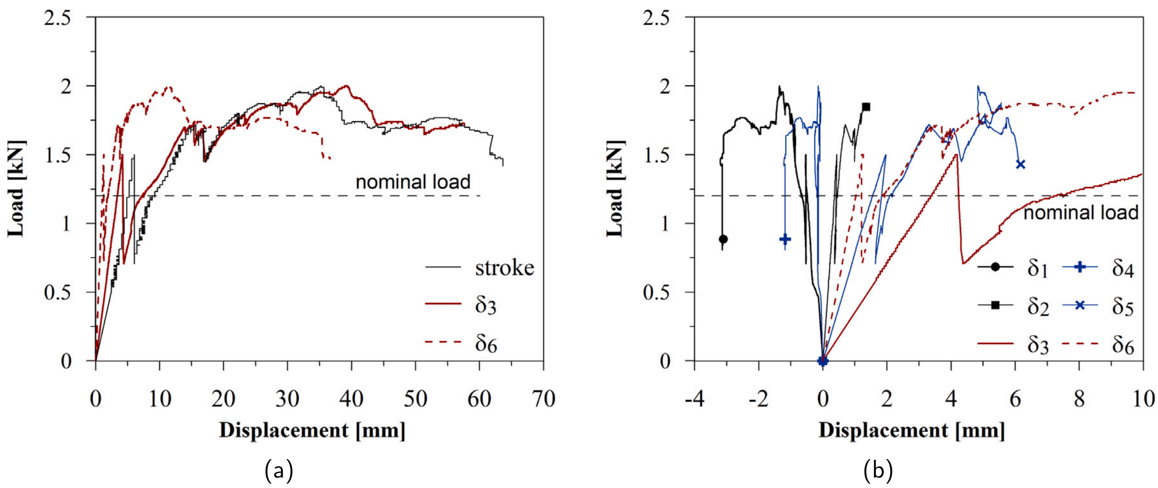

Fig. 20. Load vs. displacement curves of the eccentric load test: comparison between the stroke and $\delta_{3,6}$ (a), and plot of all δ_{1-6} (b).
Source: Adapted from [19].

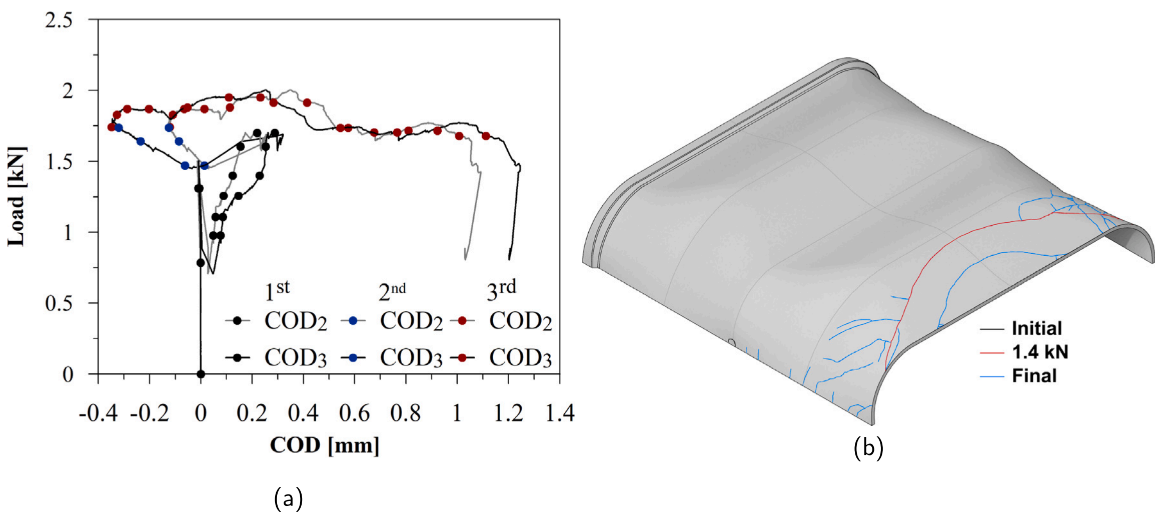

Fig. 21. Eccentric load test results: load vs. CODs (a) and crack pattern evolution during the test (b). Note that COD_1 reading was lost, while three different colors were used to help identify the $COD_{2,3}$ evolution. (For interpretation of the references to color in this figure legend, the reader is referred to the web version of this article.)
Source: Adapted from [19].

representation of the experimental behavior. Despite this limitation, the simplified model adequately captures the maximum capacity and can be considered suitable for a preliminary assessment of the structural behavior of the composite solution. The shear resistance of the full beam section was estimated with the formulation proposed by MC2010 [20] for members with conventional longitudinal bars and without specific shear reinforcement (Eq. (1)):

$$V_{Rm} = \left\{ \frac{0.18 \cdot k}{\gamma_m} \cdot \left[100 \cdot \rho_1 \cdot \left(1 + 7.5 \cdot \frac{f_{Ftu}}{f_{ct}} \right) \cdot f_{cm} \right]^{1/3} \right\} \cdot b_w \cdot d. \quad (1)$$

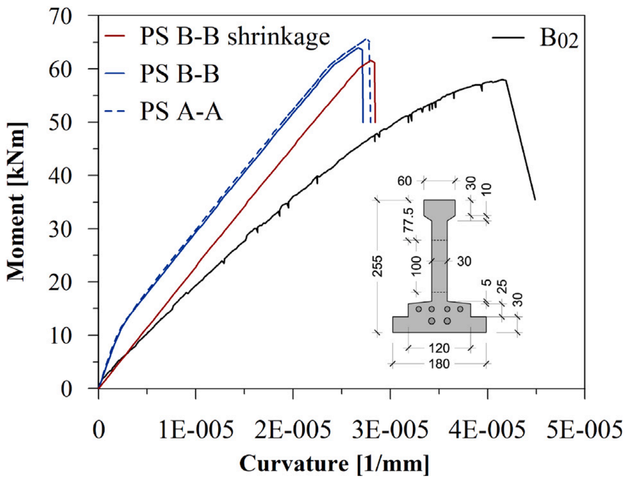

Fig. 22. Comparison between the analytical and the experimental moment vs. curvature response of the VHPFRC beam. Note: the measurements in the figure are expressed in mm.

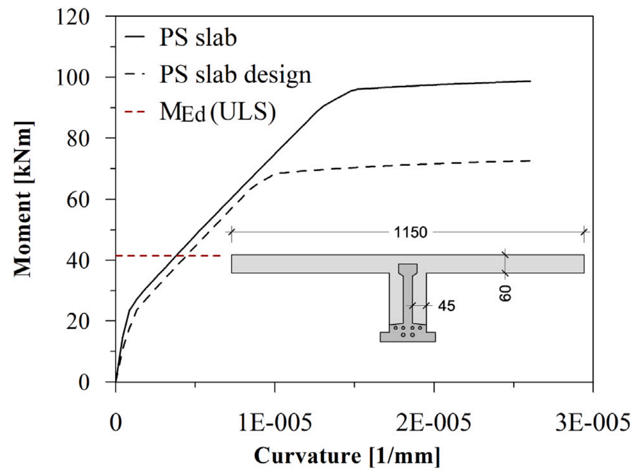

Fig. 23. Simplified estimation of the composite slab behavior and comparison with the ultimate limit state (ULS) design bending moment. Note: the measurements in the figure are expressed in mm.

An average shear resistance V_{Rm} of 48.1 kN was obtained setting the safety coefficient γ_m equal to 1 and assuming the average tensile and cylindrical compressive strengths of a C120 grade concrete (f_{ct} = 5.6 MPa and f_{cm} = 128 MPa respectively). The other introduced parameters are the effective depth (d = 233 mm), the smallest width of the cross section (b_w = 30 mm), the size-effect factor (k = 1.926), the longitudinal reinforcement ratio (ρ_l = 0.077), and the residual mean strength of the VHPFRC at a crack opening of 1.5 mm (f_{Ftu} = 5.15 MPa).

Besides underestimating the experimental response obtained by testing the beam segments (minimum of 66.5 kN reported in Section 5.2), the average shear strength V_{Rm} results higher than the analytically estimated ultimate shear V_u, corroborating the interpretation of a failure mode dominated by bending.

7.2. Structural and environmental considerations for the full composite slab

After being validated for the individually tested VHPFRC beam, the plane-section approach was extended to estimate the flexural behavior of the composite slab. Two different analyses were carried out to determine its moment vs. curvature response, identify the most probable failure mode, and estimate its maximum design capacity.

In the first case, the results of which are depicted in Fig. 23 with a solid line, the average constitutive laws used for the VHPFRC and the steel rebar were the same defined earlier for the sole prefabricated beam. In addition, the characteristic compressive and tensile laws of a C45-4b grade SFRC (according to [20] provisions) were implemented. On the other hand, in the second case (black dashed line in Fig. 23) safety material coefficients (1.5 for the cement-based materials and 1.15 for the steel bars) were introduced, to determine the design laws of all the involved materials and estimate the ultimate design moment (M_{Rd}) to be compared with the bending moment acting at the ultimate limit state (M_{Ed}). The latter, which results equal to 41.5 kN m, was evaluated considering the real geometry of the slab, see Section 2, under the hypothesis of a uniformly distributed live load of 3.0 kN/m^2 combined with structural dead loads at the ultimate limit state (ULS).

A simplified cross-section was assumed in both the analytical simulations to discretize the 1.15 m wide strip of the composite slab. The set geometry is reported in Fig. 23; as one should note, geometric simplifications were introduced on the SFRC portion, and the contribution of the TRC shell was neglected. This was partly due to the limited tensile capacity of the AR glass fabric in the weft direction, the discontinuity of the fabric between individual TRC modules, and the fact that the majority of the TRC shell is located near the neutral axis of the composite section, rendering its contribution under small displacement conditions negligible.

In both the analyses, the effect of restrained shrinkage was also neglected and the constitutive law of the steel rebar was cut at a conventional ultimate strain of 1%. For this reason, only a minor variation can be noted in the curvature values at the end of the two diagrams. In both cases, the curves terminate upon reaching this strain limit, and the absence of brittle failure modes was identified, in contrast to what was experimentally observed and analytically confirmed for the VHPFRC beam. This demonstrates that the brittle compressive failure exhibited by the single VHPFRC beam due to the high reinforcement ratio is avoided in the final application, as the additional FRC layer significantly increases the compression area, promoting a ductile failure mode. From the results of this last investigation, a safety margin of 1.8 was computed, corresponding to the ratio between the resistant (M_{Rd} = 73.9 kN m) and the acting bending moment (M_{Ed} = 41.5 kN m) at ULS.

To provide a preliminary quantitative assessment of the environmental sustainability of the proposed solution, a comparison was made with traditional concrete floor systems considered in a recent study by Broyles et al. [25]. Using the interactive web app developed in their work, embodied carbon (EC_{tot}) values were estimated for 1 m^2 of six reinforced concrete (RC) solutions and four prestressed concrete (PC) solutions. The assumptions considered were: a span L of 6 m, concrete compressive strength of 40 MPa, an applied live load of 3 kN/m^2, no applied dead load other than the structural self-weight, and a L/480 long-term deflection limit. Under these assumptions, the estimated values in the cradle-to-gate (A1–A3) life cycle assessment (LCA) stages are those collected in Table 6.

The solution proposed in this paper was evaluated using the conservative parameters reported in Table 7, which lists the various materials constituting the structural system, associated with the estimated material quantities (MQ) based on Fig. 2, and estimates of global warming potential (GWP) determined from literature data [25–27] and environmental product declarations (EPD) provided by the mix design ingredient manufacturers. The total embodied carbon (EC_{tot}) of the proposed slab is 60.1 kgCO_2e/m^2, and the normalized quantity of concrete used is 0.11 m^3/m^2.

The EC results reported in Table 7 show that, despite the higher GWP of the materials used (largely due to the increased dosages of cement, the use of superplasticizers, and steel fibers), the embodied

Table 6
Environmental impacts of material use per 1 m^2 of traditional slab systems discussed in [25], compared with the proposed solution. MQ: material quantity (normalized concrete slab volume); EC_{tot}: embodied carbon of the system.

Floor system	MQ [m^3]	EC_{tot} [$kgCO_2e$]
RC flat plate	0.24	107.61
RC flat slab	0.24	109.73
RC pan joist slab (one-way)	0.17	81.2
RC two-way slab	0.21	95.77
RC waffle slab	0.21	93.61
RC voided plate	0.19	89.76
PC flat plate	0.18	82.95
PC precast hollow core slab (one-way)	0.11	70.29
PC voided plate with orthogonal layout	0.16	74.16
PC voided plate with diagonal layout	0.16	77.36
Proposed solution	0.11	60.1

Table 7
Environmental impact of material use per 1 m^2 of the proposed structural solution in the cradle-to-gate (A1–A3) LCA stages. MQ: material quantity; GWP: global warming potential; EC: embodied carbon; EC/EC_{tot}: relative contribution to the total embodied carbon.

Material	MQ [–]	GWP [–]	EC [$kgCO_2e$]	EC/EC_{tot} [–]
FRC	8.93E–2 m^3	430 $kgCO_2e/m^3$	38.4	64%
VHPFRC	1.37E–2 m^3	790 $kgCO_2e/m^3$	10.8	18%
HPC	1.09E–2 m^3	630 $kgCO_2e/m^3$	6.8	11%
Steel (rebar)	3.69 kg	0.854 $kgCO_2e/kg$	3.2	5%
AR glass fabric	1.05 m^2	0.86 $kgCO_2e/m^2$	0.9	1%

carbon of the solution is kept low thanks to structural optimization that results in the use of reduced material volumes. The component that has the greatest impact on the EC_{tot} value (see the relative contributions in Table 7) is the supplementary FRC casting, characterized by the largest specific volume. Therefore, further benefits could be achieved by improving the environmental performance of the mix used.

From the comparison with the floor systems reported in Table 6, it can be noted that the proposed solution is comparable to the best solution analyzed in [25], which corresponds to the PC precast hollow core slab one-way system. The normalized concrete volume, and thus the structural mass of the solution, is identical, and from an environmental perspective, a similar EC is identified, allowing for a positive evaluation of the sustainability potential of the proposed system.

Despite a comparable EC_{tot} value, it is noteworthy that the imposed live load of 3 kN/m^2 is conservative. The M_{Rd} value reported in Fig. 23 is in fact oversized by a factor 1.8 with respect to M_{Ed}, and following detailed SLS and ULS checks in both longitudinal and transverse directions, it would be possible to assign a maximum live load of 7 kN/m^2 to the solution. In this scenario, the PC precast hollow core slab solution would entail MQ values of 0.15 m^3/m^2 and EC_{tot} values of 91.85 kg CO_2e/m^2, thus highlighting worse environmental performance and a greater structural mass, which in turn has secondary effects on the supporting structures of the building.

However, to fully validate the sustainability results, it would be necessary to: (i) use the same database (which currently does not include advanced cement-based materials), conducting a comparison on the average global warming potential values of the concrete mixes; (ii) account for the high variability of GWP data highlighted in [25]; (iii) use the same structural design code; and (iv) include the contribution of the primary beams of the proposed solution, which were not optimized and considered in this preliminary study. Furthermore, to provide sound conclusions, it would be appropriate to evaluate the cradle-to-grave scenario, also exploring the durability of the alternative solutions and the recycling potential of the materials used. Such detailed LCA analyses are beyond the scope of this work and are deferred to future studies.

8. Concluding remarks and future perspectives

The results underscore the application potential of high-performance cementitious materials in semi-prefabricated structural solutions, providing the dual advantages of ensuring robust mechanical performance while minimizing dead loads. Based on the presented findings, the following conclusions can be drawn:

- properly designed TRC exhibits typical trilinear strain-hardening behaviors, providing membrane and flexural responses capable of withstanding significant post-cracking stresses. Full-scale tests on TRC lost formworks subjected to both centered and eccentric point loads, yielded promising results. Geometric effects and structural redundancy help avoid local failure due to incorrect fabric placement. Satisfactory outcomes were achieved for both load combinations, highlighting the ability of thin TRC shells to ensure safety during assembly, through the activation of second-order mechanisms contributing to overall strength through the development of membrane stresses.
- The VHPFRC beam reinforced only with longitudinal rebar demonstrates significant resistance in both bending and shear. Simplified calculations prove that, owing to the contribution of fibers and alternative shear resistance mechanisms, bending failure precedes shear failure. This satisfies capacity design criteria, eliminating the necessity for conventional shear reinforcement. The brittle compressive failure of the top bulb is not a cause for concern, as in the permanent scenario the presence of finishing SFRC increases the compressed zone area, fostering a ductile flexural response.
- Analyses based on the plane-section kinematic assumption and on the MC2010 constitutive relationships provide reasonable estimates of the VHPFRC beam capacity. In this particular case, the MC2010 shear formulation for fiber-reinforced members with longitudinal rebar underestimates shear strength, ensuring a significant safety margin. For these reasons, it is believed that the simplified approaches adopted can be effectively used in the design of structural composite systems, as demonstrated by the complete elevated slab solution.
- The results demonstrate that, despite the higher GWP of the materials used, the embodied carbon of the proposed solution remains low due to efficient structural optimization. While the overall environmental impact is comparable to the lower bound of existing floor systems, the conservatively assumed live load suggests potential for increased load capacity. To fully validate the sustainability of the proposed solution, future studies should incorporate a comprehensive cradle-to-grave assessment, including detailed analysis of durability, recycling potential, and contributions from primary beams, which were not considered in this preliminary study.

Future prospects could include confirmation of the behavior of different elements through nonlinear numerical analyses. In particular, this would allow the introduction of the shear deformability of the VHPFRC beam and a more accurate simulation of both the local behavior of the TRC formwork (to evaluate, for example, the optimization of the thicknesses and fabric used) and of the entire composite slab.

CRediT authorship contribution statement

Marco Carlo Rampini: Conceptualization, Data curation, Investigation, Methodology, Software, Visualization, Writing – original draft, Writing – review & editing. **Giulio Zani:** Conceptualization, Data curation, Investigation, Methodology, Validation, Writing – original draft, Writing – review & editing. **Matteo Colombo:** Methodology, Supervision. **Marco di Prisco:** Conceptualization, Funding acquisition, Supervision, Writing – review & editing.

Declaration of competing interest

The authors declare that they have no known competing financial interests or personal relationships that could have appeared to influence the work reported in this paper.

Acknowledgments

The authors express their gratitude to Mangiavacchi Pedercini Spa for providing financial support for this research. Special thanks are extended to Dr. Alessio Caverzan, along with MEng Marco G. L. Lamperti and MEng Ezio Marchetti, for their valuable contributions to the development of this work.

References

[1] Valeri Patrick, Guaita Patricia, Baur Raffael, Fernández Ruiz Miguel, Fernández-Ordóñez David, Muttoni Aurelio. Textile reinforced concrete for sustainable structures: Future perspectives and application to a prototype pavilion. Struct Concr 2020;21(6):2251–67.
[2] Zani Giulio, Rampini Marco Carlo, Colombo Matteo, di Prisco Marco. Bending behavior of cement-based multi-layered roof elements. Eng Struct 2019;190:101–15.
[3] Zani Giulio, Pepe Marco, Rampini Marco Carlo, Michels Julien, Martinelli Enzo. Numerical modelling of innovative deconstructable shallow beams made of recycled aggregate concrete and shape memory steel reinforcement. Lect Not Civ Eng 2023;350 LNCE:685–94.
[4] May Sebastian, Michler Harald, Schladitz Frank, Curbach Manfred. Lightweight ceiling system made of carbon reinforced concrete. Struct Concr 2018;19(6):1862–72.
[5] Voo Yen Lei, Foster Stephen J. Characteristics of ultra-high performance 'ductile' concrete and its impact on sustainable construction. IES J A: Civ Struct Eng 2010;3(3):168–87.
[6] Menegatti Lucas Caon, Castrillon Fernandez Letícia Ikeda, Caldas Lucas Rosse, Pepe Marco, Pittau Francesco, Zani Giulio, Rampini Marco Carlo, Michels Julien, Toledo Filho Romildo Dias, Martinelli Enzo. Environmental performance of deconstructable concrete beams made with recycled aggregates. Sustainability 2022;14(18).
[7] Adriaenssens Sigrid. The ribbed floor slab systems of pier luigi nervi. J Int Assoc Shell Spat Struct 2013;54:127–36.
[8] Lenticchia Erica, Ceravolo Rosario, Chiorino Cristiana. Damage scenario-driven strategies for the seismic monitoring of XX century spatial structures with application to Pier Luigi Nervi's Turin Exhibition Centre. Eng Struct 2017;137:256–67.
[9] di Prisco Marco, Fehling Ekkehard, Leutbecher Torsten, Thiemicke Jenny, Toutlemonde Francois, Walraven Joost, Zani Giulio. Ultra high performance fibre reinforced concrete. In: Fibre reinforced concrete. State-of-the-art report-fib bulletin 105. Fédération internationale du béton (fib); 2022.
[10] Ruiz Rafael, Todisco Leonardo, Corres Hugo. Application of high-performance fibre reinforced concrete to precast girders for road bridges: Conceptual considerations and numerical analyses. Struct Concr 2023;24(4):4645–59.
[11] Rampini Marco Carlo, Zani Giulio, Colombo Matteo, di Prisco Marco. Mechanical behaviour of TRC composites: Experimental and analytical approaches. Appl Sci 2019;9(7).
[12] Rampini Marco Carlo, Zani Giulio, Colombo Matteo, di Prisco Marco. Stiffness degradation of textile-reinforced mortar under unloading–reloading tensile cycles. J Compos Constr 2023;27(1):04022083.
[13] Papanicolaou Catherine G, Papantoniou Ioannis C. Mechanical behavior of textile reinforced concrete (TRC) / concrete composite elements. J Adv Concr Technol 2010;8(1):35–47.
[14] Sharei E, Scholzen A, Hegger J, Chudoba R. Structural behavior of a lightweight, textile-reinforced concrete barrel vault shell. Compos Struct 2017;171:505–14.
[15] Tsangouri Eleni, Van Driessche Aron, Livitsanos Georgios, Aggelis Dimitrios G. Design, casting and fracture analysis of textile reinforced cementitious shells. Dev Built Environ 2020;3:100013.
[16] Scholzen Alexander, Chudoba Rostislav, Hegger Josef. Thin-walled shell structures made of textile-reinforced concrete. Struct Concr 2015;16(1):106–14.
[17] Scheerer Silke, Chudoba Rostislav, Garibaldi Maria Patricia, Curbach Manfred. Shells made of textile reinforced concrete -applications in Germany. J Int Assoc Shell Spat Struct 2017;58(1):79–93.
[18] Rampini Marco Carlo, Zani Giulio, Colombo Matteo, di Prisco Marco. HPFRCC beams in innovative elevated slabs: experimental characterization and modeling. In: H.W. Reinhardt GJParra-Montesinos, Garrecht H, editors. Proceedings of the 7th RILEM workshop on high performance fiber reinforced cement composites. RILEM Publication S.A.R.L.; 2015, p. 489–96.
[19] Rampini Marco Carlo, Zani Giulio, Colombo Matteo, di Prisco Marco. A unidirectional ribbed slab system with prefabricated textile-reinforced concrete shells. In: S. Gabriele, A. Manuello Bertetto, F. Marmo, A. Micheletti, editors. Lecture Notes in Civil Engineering 2024;437:837–46.
[20] CEB-FIP. Model code 2010 - volume 1. 2010.
[21] European Committee for Standardization. EN 14651:2005. Test method for metallic fibered concrete - measuring the flexural tensile strength (limit of proportionality (LOP), residual). 2005.
[22] European Committee for Standardization. EN 196-1:2016. Methods of testing cement - part 1: Determination of strength. 2016.
[23] Colombo Isabella Giorgia, Magri Anna, Zani Giulio, Colombo Matteo, di Prisco Marco. Erratum to: Textile reinforced concrete: experimental investigation on design parameters. Mater Struct 2013;46(11):1953–71.
[24] Consiglio Nazionale delle Ricerche. CNR-DT 204/2006. Istruzioni per la progettazione, l'esecuzione ed il controllo di strutture di calcestruzzo fibrorinforzato (in Italian). 2006.
[25] Broyles JM, Gevaudan JP, Hopper MW, Solnosky RL, Brown NC. Equations for early-stage design embodied carbon estimation for concrete floors of varying loading and strength. Eng Struct 2024;301:117369.
[26] Joachim L, Oettel V. Experimental investigations on the application of natural plant fibers in ultra-high-performance concrete. Materials 2024;17(14).
[27] Kromoser B, Butler M, Hunger M, Kimm M, Kopf F, Mechtcherine V, Pressmair N, Traverso M. Article of RILEM TC 292-MCC: life cycle assessment (LCA) of non-metallic reinforcement for reinforcing concrete: manufacturing, durability, dismantling, recycling and reuse: a review. Mater Struct 2023;56.